Collective dynamics and molecular interactions in liquid CO_2 by inelastic neutron scattering and computer simulations

Marco Sampoli,[1,2] Ubaldo Bafile,[3] Eleonora Guarini,[2,4] and Fabrizio Barocchi[2,4]
[1]*Dipartimento di Energetica, Università di Firenze, via S. Marta 3, I-50139 Firenze, Italy*
[2]*CNR-INFM CRS-Soft, c/o Dipartimento di Fisica, Università di Roma "La Sapienza," I-00185 Roma, Italy*
[3]*Consiglio Nazionale delle Ricerche, Istituto dei Sistemi Complessi, via Madonna del Piano 10, I-50019 Sesto Fiorentino, Italy*
[4]*Dipartimento di Fisica, Università di Firenze, via G. Sansone 1, I-50019 Sesto Fiorentino, Italy*
(Received 29 January 2009; revised manuscript received 26 May 2009; published 22 June 2009)

We report an inelastic neutron scattering determination of the dynamic structure factor of liquid carbon dioxide in the wave-vector range $3<Q<17$ nm^{-1} and molecular dynamics simulations performed using several site-site intermolecular interaction models. The comparison of neutron and simulation dynamical spectra allows effective model-potential selection. The good performance of some of the CO_2 anisotropic interaction models enables a thorough investigation of the collective properties, taking full advantage of the direct access that simulations provide to the purely translational modes of a molecular liquid. Center-of-mass collective excitations of liquid CO_2 can be fully described through a viscoelastic modeling of the second-order memory function if a free Q dependence of the parameters is allowed. The system behaves in a hydrodynamiclike way up to about $Q\simeq 5$ nm^{-1}, where the thermal relaxation has a dominant role. A rather different situation is found at higher Q, ruled by both structural and dynamical effects, namely, the rapid growth of the static structure peak, the increased damping of the Brillouin lines, and the shortening of the relaxation time. Acoustic excitations propagate up to $Q\simeq 14$ nm^{-1}, while beyond this value a transition to overdamped modes takes place.

DOI: 10.1103/PhysRevB.79.214203 PACS number(s): 61.25.Em, 61.05.fg, 61.20.Ja

I. INTRODUCTION

When dealing with simple molecular fluids of fundamental importance, one would expect their dynamical and structural properties to be already known over wide thermodynamic ranges. Indeed, this is the case of water, owing to its primary role in many fields of science. Similarly, hydrogen, with its manifold applications on one side and its quantum behavior on the other, has been actively studied throughout the years by theoretical, experimental, and simulation methods.

Still, significant gaps affect the existing information on simple molecular fluids. Quite surprisingly, a property as crucial as the dense-liquid dynamic structure factor $S(Q,\omega)$ has been rarely investigated. For instance, one finds in the literature only one inelastic neutron scattering (INS) and molecular dynamics (MD) simulation study of (deuterated) methane,[1] two inelastic x-ray scattering (IXS) studies of the collective motions in ammonia,[2,3] and only a few INS (Refs. 4 and 5) and IXS (Ref. 6) investigations of liquid nitrogen. Besides water,[7–9] few other simple polyatomic liquids have attracted experimental attention: methanol,[10,11] sulfur dioxide,[12] carbon tetrachloride,[13] and more recently hydrogen and deuterium fluoride.[14,15]

The role played by neutron scattering in investigations of the intermolecular potential of fluids is witnessed by studies of static[16–24] and dynamic[25–28] properties of monatomic liquids and gases. Neutron diffraction was proven effective also on the simplest molecular fluids.[29–37] More recently, however, it was demonstrated[38] that, for a canonical molecular liquid such as methane, joint INS and MD determinations of $S(Q,\omega)$ can be very powerful in the analysis and discrimination of anisotropic intermolecular potentials. Thus, while limited knowledge of the behavior of simple molecular liquids at the nanometer and picosecond length and time scales would by itself motivate new experiments and simulations, an even more stimulating reason for studying the dynamics of these systems comes from the possibility of probing their anisotropic interactions, with the additional goal of understanding similarities and differences among different fluids. Indeed, we have shown in a very recent short publication[39] that such an approach is successful also in the case of liquid carbon dioxide, where the sensitivity of $S(Q,\omega)$ spectra to the details of the interaction potential is again confirmed.

When performed with experimentally validated potentials, MD simulation is a unique powerful method for deep and reliable analyses of important dynamical quantities that are difficult or impossible to obtain from experiment, such as the center-of-mass (CM) dynamic structure factor, the self- and collective rotational dynamics, and so on. Indeed, in the mentioned methane case, the usefulness of the INS-MD approach was not limited to the selection of a realistic anisotropic potential able to account for the observed high-resolution spectra at Q values ranging from ~ 0.1 to $\sim 0.8Q_p$, with Q_p as the position of the main maximum in the static structure factor [in CD_4, $Q_p=19$ nm^{-1} (Ref. 40)]. In fact, MD results based on the best potential also allowed extension of the analysis of the translational excitation modes to (Q,ω) domains outside the experimental range, i.e., at Q values up to $Q\sim 4Q_p$.[41]

Such evidence of the wealth of information attainable through coupled INS-MD enquiries on the dynamics of simple polyatomic liquids is the basis of the present study of dense-liquid CO_2, extending the results of Ref. 39. We give here a complete account of the INS measurements and MD results and exploit them for an in-depth analysis of the trans-

lational collective picosecond dynamics and of the sound propagation properties of dense-liquid CO_2 for which only $S(Q)$ structural studies can actually be retraced in the literature.[29–31] Beyond the novelty obviously presented by the first determination of whatsoever important property of a system [$S(Q,\omega)$ in this case], a more specific reason of interest in CO_2 is the stronger anisotropic character of interactions in this fluid compared with the methane case. Also, the simple triatomic linear structure of the carbon dioxide molecule keeps the attainment of our scientific goals easy enough from the data analysis point of view.

On the INS experimental side, carbon dioxide is an ideal sample for its extremely low absorption and, mainly, its negligible incoherent-to-coherent ratio of neutron cross sections (less than 1 part per 1000) for both carbon and oxygen.[42] The absence of incoherent scattering greatly simplifies the experimental access to the collective properties. In addition, the relatively low adiabatic sound velocity c_s of dense-liquid CO_2 ($c_s \sim 940$ m s^{-1}, Ref. 43) allows exploitation of the good energy resolution (better than 1 meV) attained with thermal neutron spectrometers.

The paper is organized as follows. In Sec. II details of the INS measurements and data treatment are given. Section III describes the simulation work based on a number of anisotropic potentials proposed for CO_2. The INS and MD results are compared and commented on in Sec. IV, where site-site models able to properly account for the INS data in our Q range can readily be identified. The MD data based on the best validated pair potential were finally used, in Sec. V, for a reliable and detailed analysis of the CM spectra, carried out in the framework of a viscoelastic (VE) description. Our concluding remarks can be found in Sec. VI.

II. EXPERIMENT AND DATA ANALYSIS

The inelastic neutron scattering spectra of liquid CO_2 were collected using the three-axis spectrometer IN3 of the Institut Laue-Langevin in Grenoble. Constant-Q energy scans were performed at eight Q values between 3 and 17 nm^{-1}, with the maximum Q corresponding to $\sim 0.9Q_p$. ($Q_p \simeq 19$ nm^{-1} for a CO_2 state similar to ours.[29]) An inverse-geometry configuration of the instrument was adopted to perform scans in energy transfer $E=E_0-E_1$, with fixed final energy $E_1=14.7$ meV and variable incident energy E_0 (maximum E_0 variation between $\sim E_1/2$ and $1.8E_1$). Incident and final neutron energies were selected by using the Cu(111) and pyrolitic-graphite(002) Bragg reflections of the monochromator and analyzer crystals, respectively. The rather relaxed setup chosen for the collimation stages from the monochromator to the detector $(40',40',60')$ corresponds to a reasonable compromise between an acceptable scattered intensity and a suitable energy resolution. In fact, the rather low E_1 value required to properly probe the acoustic modes of CO_2 allows one to avoid extreme collimations. Further, for such a specific E_1 value it is well known in neutron practice[44,45] that a graphite filter can be used in the scattered beam for suppression of higher-order harmonics from the analyzer.

The sample gas was liquefied at $T=221.9\pm0.3$ K directly inside a cylindrical vanadium container, with inner diameter of 11.35 mm and wall thickness of 0.1 mm, placed inside a cryostat and connected to an external gas-handling system. A large vacuum box (1 m diameter) surrounded the cryostat tail to minimize the scattering from air along the incident and scattered paths. During the measurements the gas pressure was maintained at an average value of $p=1.01\pm0.03$ MPa in order to keep the CO_2 sample in the single-phase liquid state of molecular number density[43] $n=15.88\pm0.01$ nm^{-3}, which is $\sim 1\%$ lower than that of the triple point. Such a density, combined with the scattering and absorption properties of carbon dioxide ($\sigma_{scat}=14.02$ b and $\sigma_{abs}=5\times10^{-3}$ b for 14.7 meV neutrons,[42] with 1 b $=10^{-10}$ nm^2) and the shape of the sample, corresponds to a neutron scattering power of about 18%, which also implies that multiple-scattering effects are still treatable with reasonable accuracy.

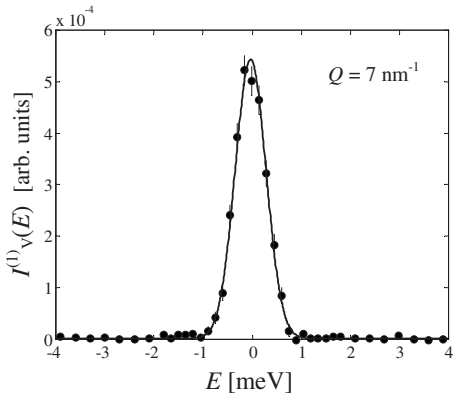

FIG. 1. Single scattering intensity of the vanadium empty can at $Q=7$ nm^{-1} (full circles with error bars) and Gaussian fit to the data (solid curve).

In addition to the sample runs, usual background measurements have been performed, including empty can, empty cryostat (plus vacuum box), and absorbing cadmium sample. The empty vanadium can runs, once corrected for the various effects influencing the measurements (e.g., background, multiple scattering, and self-attenuation), also provided us with the necessary data for an experimental estimate of both the absolute normalization factors pertaining to the chosen instrumental setup and the elastic energy resolution. On the one hand, the corrected vanadium integrated intensities provided the required link between experimental and absolute quantities, thanks to the knowledge of the mainly elastic and totally incoherent neutron scattering law of such a special sample. On the other hand, the spectral distribution turned out to be well described by the Gaussian behavior typical of the elastic resolution function in neutron scattering. In particular, the Gaussian fits to the vanadium data yielded a spectral full width at half maximum of 0.74 meV, independent of Q within the experimental uncertainties, in agreement with previous energy-resolution measurements on IN3 with the same setup.[46] An example of a vanadium spectrum, along with its Gaussian fit curve, is reported in Fig. 1 for $Q=7$ nm^{-1}.

The interesting dynamical features of a coherent scattering measurement are contained in the single-scattering absorption-free intensity from the sample, $I(Q,\omega)$, obtained

through the application of the typical corrections required in neutron-data treatment and commented on later in this section. However, in the molecular case, this quantity does not simply mirror the density-density fluctuation spectrum, i.e., the usual $S(Q,\omega)$. In a (single-component) molecular fluid, the dynamic structure factor *per molecule* can be written as

$$S(Q,\omega) = \sum_{\alpha,\beta} \sqrt{n_\alpha n_\beta} S_{\alpha\beta}(Q,\omega), \tag{1}$$

where α and β run over the atomic species present in the system, n_α is the number of atoms of species α in one molecule, and the *partial* dynamic structure factors $S_{\alpha\beta}(Q,\omega)$ are introduced according to the Ashcroft-Langreth[47] definition.

However, the coherent signal recorded in an INS experiment is related to a different combination of the partial dynamic structure factors. In the present case, where constant-monitor scans in inverse-geometry operation of a three-axis neutron spectrometer were performed, the following proportionality relation holds, in particular, to a very good approximation:[46]

$$I(Q,\omega) \propto \tilde{S}^{\text{expt}}(Q,\omega), \tag{2}$$

where the superscript "expt" is used to synthetically recall that measured spectra also reflect detailed-balance asymmetry and experimental resolution broadening. These effects modify the symmetrical $\tilde{S}(Q,\omega)$ which defines the appropriate "neutron" combination of the partial $S_{\alpha\beta}$ actually probed by coherent neutron scattering. The latter is given by

$$\tilde{S}(Q,\omega) = \sum_{\alpha,\beta} \sqrt{n_\alpha n_\beta} b_{\text{coh}}^{(\alpha)} b_{\text{coh}}^{(\beta)} S_{\alpha\beta}(Q,\omega) \tag{3}$$

and directly depends on the coherent scattering lengths $b_{\text{coh}}^{(\alpha)}$ of the atomic species in the sample. For CO_2, the above expression corresponds to

$$\tilde{S}(Q,\omega) = b_{\text{coh}}^{(\text{C})2} S_{\text{CC}}(Q,\omega) + 2\sqrt{2} b_{\text{coh}}^{(\text{C})} b_{\text{coh}}^{(\text{O})} S_{\text{CO}}(Q,\omega) + 2 b_{\text{coh}}^{(\text{O})2} S_{\text{OO}}(Q,\omega) \tag{4}$$

where we took into account that $S_{\alpha\beta}=S_{\beta\alpha}$.

As evident from Eqs. (2) and (3), the partials cannot be separately probed in a single neutron experiment and are seen globally by neutrons as the result of a linear combination marked by the probe fingerprints. Apart from the specific weights, the same happens for IXS measurements on molecular samples. Thus, INS and IXS methods actually provide strictly probe-dependent combinations of the partial $S_{\alpha\beta}$, while the dynamic structure factor $S(Q,\omega)$ defined in Eq. (1) remains inaccessible unless the different species in the sample have equal scattering cross sections.

This fact does not of course diminish the importance of spectroscopic measurements for comparisons with theories and/or simulations since the latter can provide each partial $S_{\alpha\beta}$ once an interaction model is adopted. Therefore, useful comparisons with experiment can be performed by referring to the theoretical or simulation equivalents of the experimental $\tilde{S}^{\text{expt}}(Q,\omega)$, i.e., by combining the calculated partials with the appropriate cross-section factors and by taking asymmetry and resolution effects into account.

In any case, determination of $\tilde{S}^{\text{expt}}(Q,\omega)$ from the raw neutron intensities requires some work also in conditions as favorable as the present ones, where incoherent scattering is negligible and the instrument setup and operation mode lead to the simple relation of Eq. (2) to within an experimental normalization factor. In particular, corrections for attenuation and size effects, multiple and container scattering, and environmental background need to be applied to the raw scattering data in order to extract $I(Q,\omega)$ and, via final data normalization, $\tilde{S}^{\text{expt}}(Q,\omega)$. In addition, specific instrument–related effects must also be considered, according to the spectrometer in use.

The neutron-data analysis for the determination of $I(Q,\omega)$ has been performed by following correction methods very similar to those detailed in Ref. 46, allowing, in addition, for the presence of a cryostat as an extra source of background. Moreover, the modeling of the scattering law of the sample, *a priori* required for an optimized estimate of multiple scattering, had to be modified in passing from a dilute "incoherent" gas[46] to the present dense "coherent" liquid. We concentrate here on the latter point, which is less trivial than an appropriate background schematization.

Multiple scattering is corrected for by the method sketched in Ref. 46, which has the advantage to be applicable independently of the actual units of the experimental intensities. We evaluated, at each (Q,ω) point, the intensity of single and double scatterings through Monte Carlo integration, taking into account the actual geometry of the experimental setup. (Neutrons scattered three or more times before reaching the detector contribute to the measured signal to a negligible extent, given the scattering power of the sample.) The distribution of deviation angles in each event of a multiple-scattering sequence, as determined from the Monte Carlo calculations, shows that in most cases rather high values (greater than 70°) are involved, as is to be expected from solid-angle considerations. These correspond to exchanged wave vectors typically exceeding 40 nm^{-1} (i.e., $>2Q_p$). Thus, in the evaluation of multiple-scattering contributions involving the sample, and characterized by such high-Q individual processes, we used the single-molecule free-rotor dynamic neutron cross section of CO_2, which can be accurately modeled through proper quantum-mechanical calculations[48] with methods similar to those described in Ref. 49.

A more delicate point is the parallel estimate of the single-scattering intensity needed to establish the ratio of multiple-to-single events. Single-scattering calculations require an *a priori* modeling of the (unknown) $\tilde{S}(Q,\omega)$ of liquid CO_2 at the same Q values probed in the measurements. At such wave vectors, the dynamics of liquid CO_2 strongly differs from that of the free-particle fluid of triatomic vibrating rotors assumed for higher-order (and far higher-Q) scattering events. Other possible schematizations of the scattering law (e.g., based on simple self-diffusion or linearized hydrodynamics[50]) are also inappropriate. In fact, *distinct* intermolecular correlations are by no means negligible nor can

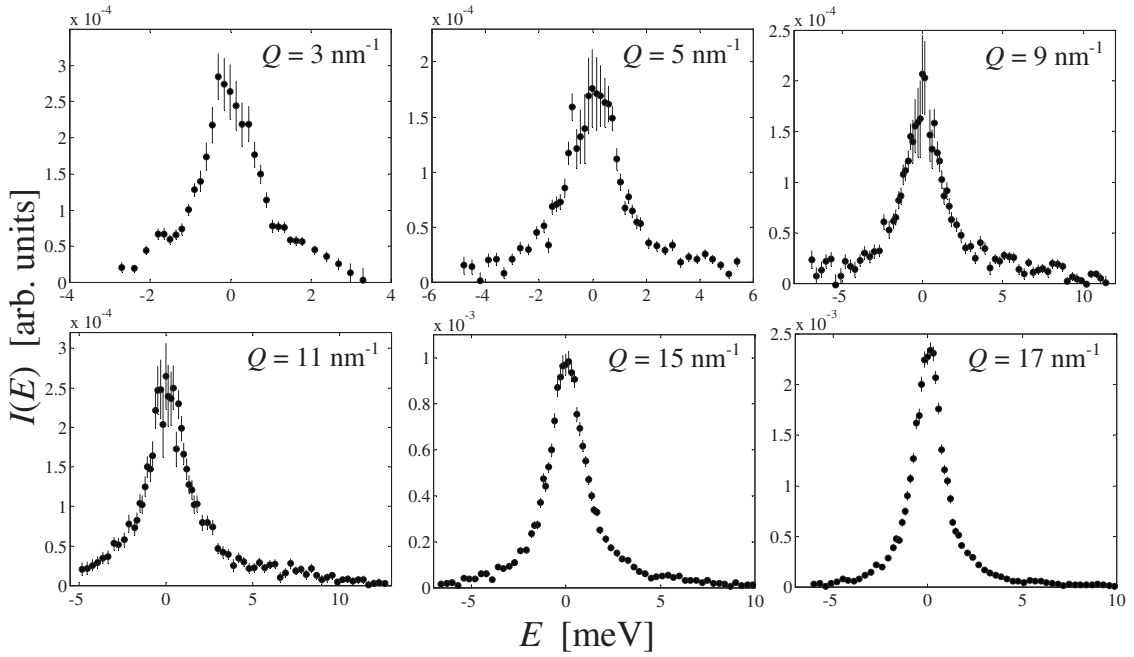

FIG. 2. $I(Q,E)$ of liquid CO_2 at various experimental Q values (full circles with error bars).

hydrodynamic theory confidently be used to model them in the whole Q range of our experiment, where deviations from hydrodynamic behavior are expected. Thus, the best way to reasonably evaluate the single scattering from the sample is to use, as a realistic scattering law for the Monte Carlo integrations described in Ref. 46, the MD $\tilde{S}(Q,\omega)$. Details about the MD simulations and reliable model potentials will be given in the remainder of this paper. At this stage of the analysis, MD data have only been employed to estimate part of a correction, i.e., the denominator of the frequency-dependent multiple-to-single-scattering ratio, and no significant difference was found between the estimates obtained with any of the four potentials that give spectra in good agreement with the experimental ones, as explained in Sec. IV. Differently, the estimate of the numerator could reliably be performed in an independent way, without needing to resort to the MD predictions. As expected, the multiple-scattering contribution evaluated with this procedure progressively reduces with increasing Q, with nearly negligible importance at the upper limits of our Q range.

With these correction methods we could derive the fully corrected single-scattering intensity $I(Q,\omega)$ shown in Fig. 2. Vanadium normalization finally allowed determination of $\tilde{S}^{\text{expt}}(Q,\omega)$ in absolute units, as required for comparison with the MD results. The uncertainties on the densities and illuminated volumes of both the CO_2 and vanadium samples, as well as on the integrals of the vanadium spectra, were estimated to lead to an overall 6% relative error on the experimental calibration. As a necessary check of the normalization procedure, the low-Q trend of the $\tilde{S}(Q)$ data (obtained by frequency integration of the spectra) was compared with the $Q=0$ thermodynamic prescription. In this respect, we note that with the Ashcroft-Langreth definition of the partial $S_{\alpha\beta}(Q,\omega)$ one obtains, at $Q=0$, the following identities in the CO_2 case: $S_{\text{CO}}(0,\omega)=\sqrt{2}S_{\text{CC}}(0,\omega)$ and $S_{\text{OO}}(0,\omega)=2S_{\text{CC}}(0,\omega)$. Thus, the $Q=0$ limit of Eq. (4) can be written in terms of the CC term only as

$$\tilde{S}(0,\omega)=(b_{\text{coh}}^{(\text{C})}+2b_{\text{coh}}^{(\text{O})})^2 S_{\text{CC}}(0,\omega). \tag{5}$$

The zeroth moment of Eq. (5) is $\tilde{S}(0)=(b_{\text{coh}}^{(\text{C})}+2b_{\text{coh}}^{(\text{O})})^2 n\chi_T k_B T$, where k_B is the Boltzmann constant and χ_T is the isothermal compressibility of our CO_2 state.[43] The comparison between the experimental $\tilde{S}(Q)$ and the $\tilde{S}(0)$ thermodynamic value will be postponed to include also the MD results.

III. MOLECULAR DYNAMICS SIMULATIONS OF LIQUID CO_2

The microscopic dynamics of the CO_2 sample was simulated in the Q range between 2 and 17 nm^{-1}, using six different models for the site-site interactions, in a constant-*NVE* ensemble containing 500 rigid molecules. All the potentials (energy and derivatives) were tabulated to speed up the calculation of the forces (the force cutoff distance was at half the box length, about 1.6 nm). The equations of motion were integrated, using a time step of 1.67 fs, with the Verlet and Fincham[51] algorithms for translations and rotations, respectively. The energy conservation condition was more than satisfactorily fulfilled as a relative drift of about 2×10^{-5} was achieved over 1000 time steps.

After a thermalization interval lasting more than 200 ps, the time evolution of the system was followed for about 1 ns and the configurations stored every 6 time steps, i.e., every 10 fs. The $S_{\alpha\beta}(Q,\omega)$ were calculated from the power density spectrum of the corresponding signals (with Welch periodograms and Hanning windows) and averaged over all the equivalent directions corresponding to the same $|\mathbf{Q}|$.

The six anisotropic potentials we employed are those of Murthy *et al.* (MSM),[52] Harris and Yung (EPM2),[53] Tsuzuki

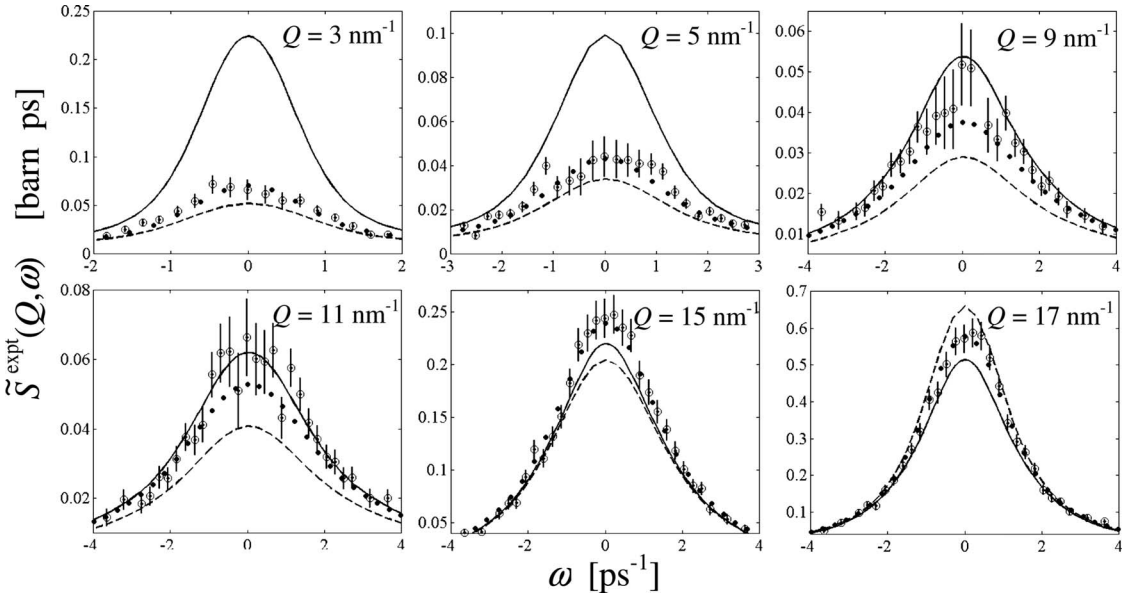

FIG. 3. Central peak of the experimental $\tilde{S}^{\mathrm{expt}}(Q,\omega)$ of liquid CO_2 (circles with error bars) at various experimental Q values compared with the MD spectra obtained with the EPM2 (full dots), BBV (solid), and TT (dashed) potentials.

and Tanabe (TT),[54] Bock *et al.* (BBV),[55] Potoff and Siepmann (TraPPE),[56] and Zhang and Duan (ZD).[57] Two of these, TT and BBV, are based on *ab initio* calculations. Most abbreviations follow those adopted in Ref. 57 where the proposed ZD interaction model is accompanied by a careful review of other three-center potentials for CO_2. In addition to the detailed and useful discussion in Ref. 57 about merits and defects of the various models, few remarks are worth noting. As also stated in a recent work by Nieto-Draghi *et al.*[58] scarce attention has generally been devoted, for model testing, to dynamic quantities, typically limited to the self-diffusion coefficient.[57] In this context, our work partly aims at reinforcing the importance of appreciable efforts as those of Ref. 58, where the prediction of quantities such as thermal conductivity λ and shear viscosity η_s of CO_2 was verified by simulations, in various thermodynamic conditions, at least for one model (EPM2). Here, in a somewhat complementary way to Ref. 58, restricting ourselves to only one liquid state but extending our MD study to several potentials, we address a quantity, the dynamic structure factor, which is a more complex outcome of the mixing of several thermodynamical and transport properties of a fluid, including thermal conductivity λ, shear viscosity η_s, bulk viscosity η_b, thermal diffusivity D_T, and specific heats ratio γ_0.[50]

IV. COMPARISON OF INS DATA WITH MD RESULTS

As mentioned, experimental spectra carry the fingerprints of both the detailed-balance condition and the energy-resolution limitations of the spectrometer. It is widely accepted that the most sensible way to compare experimental data with (classical) resolution-free models or high-resolution simulations is to keep the data as the main reference (without attempting at deconvolution) and to apply the detailed-balance asymmetry and the experimental resolution broadening to model-calculated or simulated spectra. In this section, therefore, asymmetric and resolution-broadened experimental and simulated spectra will be displayed. The detailed balance has been included through the frequency-dependent factor $(\hbar\omega/k_BT)/[1-\exp(-\hbar\omega/k_BT)]$.

Also, in order to follow the notation and units often adopted in other papers, we will, from now on, plot experimental and simulated quantities as a function of the angular frequency ω, instead of $E=\hbar\omega$, though the latter notation was preferred in Figs. 1 and 2 to facilitate an immediate understanding of the experimental ranges and related instrument setup by neutron experimentalists.

The comparison between the experimental $\tilde{S}^{\mathrm{expt}}(Q,\omega)$ of liquid CO_2 and the MD simulation results for the various potential models was graphically displayed in Ref. 39. Here, in order to have a measure of the level of agreement with experimental results, we calculated, for the various potentials, the value of $\Delta=\langle(1/N)\Sigma_i w_i(S_i^{\mathrm{meas}}-S_i^{\mathrm{sim}})^2\rangle$ where, for each Q, the index i runs over the measured spectral points, S_i^{meas} and S_i^{sim} are shorthand notations for the spectral intensities at frequency ω_i, the weights w_i are the inverse squared experimental uncertainties, and N is the number of points in the spectrum. The angular brackets indicate that the results are finally averaged over all investigated Q values. The EPM2, MSM, ZD, and TraPPE produce quite similar spectra, in overall rather good agreement with the neutron data. Their Δ values are 1.27, 1.33, 1.34, and 1.56, respectively. In contrast, the TT (Δ=2.88) and BBV (Δ=9.63) simulated data clearly deviate (with opposite tendencies) from experiment at low and intermediate wave vectors. For both models, the discrepancies mainly regard the quasielastic peak. In Fig. 3 we show the detail of the main peak in the EPM2 case (taken as a representative of the group of better-performing models) and for the two most disagreeing models, BBV and TT. The BBV overestimate of the quasielastic line progressively reduces as Q grows and is finally reversed into an underesti-

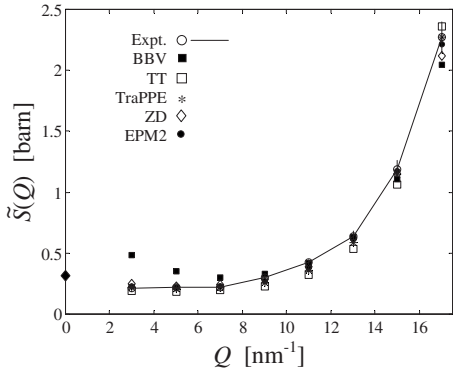

FIG. 4. $\widetilde{S}(Q)$ obtained by frequency integration of the inelastic neutron data (circles with error bars connected by a solid line) and of the simulated spectra: ZD (diamonds), EPM2 (full dots), TraPPE (stars), TT (empty squares), and BBV (full squares). The full diamond at $Q=0$ is the thermodynamic limit (see text). Experimental error bars, smaller than the size of the symbols at Q values below 11 nm^{-1}, take into account the uncertainties on both the normalization and spectral integration procedures.

mate at the two highest-Q values. Conversely, the TT underestimate of the main peak, visible at most wave vectors, is eventually changed into a slight overestimate at 17 nm^{-1}.

The frequency integrals of the neutron and MD spectra also reflect the overall relative behaviors commented above. The static $\widetilde{S}(Q)$ data can be analyzed in Fig. 4. One can note the good consistency of the experimental $\widetilde{S}(Q)$ with the expected $\widetilde{S}(0)$ thermodynamic value. Also, the EPM2, ZD, and TraPPE MD-derived $\widetilde{S}(Q)$ agree well with the experimental one. Conversely, the limited but systematic underestimate of the experimental data produced by the TT model clearly affects its $\widetilde{S}(Q)$ at most Q values. The BBV deviations at low Q are much more evident, and the analysis of the zeroth frequency moment directly reveals that the BBV small-Q structure is irreconcilable with the $Q=0$ compressibility limit. Hence, the BBV schematization of long-range forces is likely inappropriate.

From the comparisons of Figs. 3 and 4, anisotropic CO_2 potentials able to account for experiment are thus confidently discerned from less realistic ones. The above analysis has led us to the choice of EPM2 for the collective dynamics study described in the following section. For this investigation, the MD data already presented have been supplemented with more spectra, simulated in the Q range between 1.4 and 6.4 nm^{-1} with 4000 particles and better frequency resolution. The following analysis of the collective dynamics is based on the use of both sets of MD results.

V. DYNAMICS OF TRANSLATIONAL COLLECTIVE MODES

In the case of a molecular liquid, we saw that the spectrum of the total pair correlation function of density fluctuations, i.e., the dynamic structure factor, is a combination of the various atom-atom $S_{\alpha\beta}(Q,\omega)$. All degrees of freedom of the molecular system (translational, rotational, etc.) contribute to this quantity and cannot be easily separated in most cases.

On the other hand, the theories of microscopic liquid dynamics,[50] relating spectral properties to the heat, sound, and other modes of the fluid, are "monatomic theories," where only purely translational atomic motions determine the dynamical behavior.

Generalization to the molecular case is not straightforward as soon as the particles of the fluid are no longer single atoms but (more or less complex) polyatomic units able also to rotate, vibrate, librate, and so on. Indeed, no line-shape model has ever been proposed to account for total correlation spectra of molecular fluids [Eq. (1)].

Trying to access the partial dynamic structure factors is certainly a first step to attempt possibly simpler spectral analysis. Nonetheless, each $S_{\alpha\beta}(Q,\omega)$ still carries, in general, the fingerprints of both translational and other molecular motions for which no overall model line shape is once again available.

The theoretical framework on the dynamics of collective modes and the information attainable with the present modeling tools can however be preserved for molecular fluids by addressing the quantity which more directly reflects the translational collective behavior in a monatomiclike sense, i.e., the CM dynamic structure factor.

The study of the CM dynamics appears as the only sensible way of probing the translational cooperative motions of molecular units sustaining wave propagation in the fluid, with minimized effects due to the intramolecular dynamics. In particular, use of available model line shapes for the dynamic structure factor of monatomic systems[50,59] is better justified in the molecular case when the CM motions are considered, and the relevant dynamical parameters maintain their physical meaning without being altered by the effects of the internal degrees of freedom. Moreover, such an approach facilitates comparisons among different molecular liquids, as well as with monatomic fluids.

Experimental dynamical results on molecular systems rarely refer or are reduced to the CM spectra. Despite this fact, data are often analyzed by applying the concepts (and models), uniquely developed for the $S(Q,\omega)$ of monatomic systems, to what we defined here as $\widetilde{S}(Q,\omega)$ for a molecular fluid. Such direct procedures are not rigorous because they make use of an experimental quantity influenced (except in very special cases) by both the intramolecular dynamics and the probe itself.

Certainly, the experimental determination of the CM dynamic structure factor is not trivial in the most frequent situation, where only a single measurement can be performed with a probe sensitive to all atomic species in the sample. In some case, it can approximately be determined by combining experiment with theoretical calculations, as done, e.g., for CD_4.[1] In some other case, it can be an approximate but direct output of experiment, as for NH_3 by x rays[2,3] since one atom (N), roughly coinciding with the CM, has a much larger cross section for this probe than the others (H). However, the latter fortunate combination is not common in spectroscopic studies of molecular systems.

MD simulations allow bypass of the limitations imposed by experiment as soon as a reliable interaction model is

available, and the experimental results well validate its effectiveness in the prediction of dynamical spectra. This, as we showed, is the case of CO_2. Given the good performance of the EPM2 potential, we will refer in this section to the simulation data obtained with this model, trying to reach some knowledge about the collective behavior of this fluid through a detailed study of the carbon-carbon (CC) partial dynamic structure factor, which for CO_2 is the CM one.

We analyze the $S_{CC}(Q,\omega)$ data obtained from the EPM2-based simulations in the framework of a VE modeling of the (second-order) memory function.[50] This choice is motivated by the fact that this model has been proven to account, with good accuracy, for the collective dynamics of a variety of fluids in a wide range of Q. In particular, the line shape derived from it was successfully employed as a fit function to describe the center-of-mass dynamic structure factor of (deuterated) methane.[41,59] In the present CO_2 case, the VE model turns out to be the simplest one that is able to describe correctly the simulation data at all investigated Q values.

The theoretical treatment based on a second-order memory function $M(Q,t)$, here recalled from Ref. 59 keeping the same notation used there, leads to a Langevin-type equation for the time evolution, at constant Q, of the intermediate scattering function (upper dots denote time derivatives),

$$\ddot{F}_{CC}(Q,t) + \int_0^t dt' M(Q,t-t')\dot{F}_{CC}(Q,t') + \langle\omega_Q^2\rangle F_{CC}(Q,t) = 0.$$

Through the use of Laplace transforms (here denoted by capped variables) and with initial conditions $F_{CC}(Q,0) = S_{CC}(Q)$ and $\dot{F}_{CC}(Q,0)=0$, this equation is solved to give

$$\frac{\hat{F}_{CC}(Q,z)}{S_{CC}(Q)} = \left[z + \frac{\langle\omega_Q^2\rangle}{z + \hat{M}(Q,z)} \right]^{-1}. \tag{6}$$

The viscoelastic model of $M(Q,t)$ is expressed as[50,59]

$$M(Q,t) = \Delta_L^2(Q)\exp[-t/\tau(Q)] + (\gamma(Q)-1)\langle\omega_Q^2\rangle\exp[-\Gamma_T(Q)t], \tag{7}$$

where $\langle\omega_Q^2\rangle = k_B T Q^2/mS_{CC}(Q)$ is the normalized second frequency moment of the dynamic structure factor, m is the molecular mass, and $\Delta_L^2(Q) = \omega_L^2(Q) - \gamma(Q)\langle\omega_Q^2\rangle$, with $\omega_L^2(Q)$ defined as the ratio of fourth to second spectral moment.

Before describing the meaning of the other parameters in Eq. (7), we derive the spectrum shape. Upon insertion of the Laplace transform of Eq. (7), Eq. (6) can be written as $\hat{F}_{CC}(Q,z)/S_{CC}(Q) = V(z)/W(z)$,[59] where V and W are, respectively, a third- and a fourth-degree polynomial in the complex variable z with real Q-dependent coefficients. At each Q, if z_j (with $j=A,B,C,D$) are the four solutions of the equation $W(z)=0$, one also finds[59]

$$\frac{\hat{F}_{CC}(Q,z)}{S_{CC}(Q)} = \sum_j \frac{I_j}{z - z_j}. \tag{8}$$

For ease of notation, in the following we shall omit to indicate the explicit Q dependence of I_j and z_j. Two roots, labeled as z_A and z_B, can be complex conjugate. This surely happens at low Q, in agreement with the experimental evidence of the presence of propagating modes, and in that case we write $z_A = -z_s + i\omega_s$ and $z_B = -z_s - i\omega_s$, with the corresponding amplitudes I_A and I_B also forming a pair of complex conjugate quantities. Then, since the normalized spectrum is given by[50]

$$\frac{S_{CC}(Q,\omega)}{S_{CC}(Q)} = \frac{1}{\pi}\mathrm{Re}\frac{\hat{F}_{CC}(Q,i\omega)}{S_{CC}(Q)},$$

the viscoelastic memory function is shown to lead to a spectral shape of the kind,

$$S_{CC}(Q,\omega) = \frac{S_{CC}(Q)}{\pi}\left[I_1\frac{z_1}{z_1^2+\omega^2} + I_2\frac{z_2}{z_2^2+\omega^2} + I_s\frac{z_s + b_s(\omega+\omega_s)}{z_s^2+(\omega+\omega_s)^2} + I_s\frac{z_s - b_s(\omega-\omega_s)}{z_s^2+(\omega-\omega_s)^2}\right]. \tag{9}$$

Here, subscripts 1 and 2 label the amplitudes and half widths at half maximum of two central Lorentzian lines, while "s," meaning *sound*, denotes the amplitude and width of the side lines centered at the excitation frequencies $\pm\omega_s$. Moreover, $z_1 = -z_C$ and $z_2 = -z_D$, and the amplitudes obey the relationship $I_1 + I_2 + 2I_s = 1$, with $I_1 = I_C$, $I_2 = I_D$, and $I_s = \mathrm{Re}\, I_A = \mathrm{Re}\, I_B$. The asymmetry factor b_s, distorting the pure Lorentzian shape of the inelastic lines, is

$$b_s = -\frac{\mathrm{Im}\, I_A}{\mathrm{Re}\, I_A} = \frac{1}{\omega_s}\left(\frac{I_1 z_1 + I_2 z_2}{1 - I_1 - I_2} + z_s\right).$$

Spectrum (9) corresponds to the intermediate scattering function

$$\frac{F_{CC}(Q,t)}{F_{CC}(Q,0)} = I_1 e^{-z_1 t} + I_2 e^{-z_2 t} + 2I_s e^{-z_s t}\frac{\cos(\omega_s t - \phi)}{\cos\phi} \tag{10}$$

containing two exponentially decaying terms plus an exponentially modulated oscillation, with $\tan\phi = b_s$.

At very low Q, the VE memory function reads as

$$M(Q,t) = (\nu Q^2/\tau_0)\exp(-t/\tau_0) + (1 - 1/\gamma_0)c_s^2 Q^2 \exp(-\gamma_0 D_T Q^2 t). \tag{11}$$

Such an expression is obtained by replacing $\langle\omega_Q^2\rangle$ with its $Q\to 0$ behavior $k_B T Q^2/mS_{CC}(0) = c_s^2 Q^2/\gamma_0$ and requiring that, in the $Q\to 0$ limit, the appropriate hydrodynamic description be obtained, which produces the well-known Rayleigh-Brillouin triplet line shape experimentally demonstrated in very-low-Q spectroscopic studies. In Eq. (11), ν is the longitudinal kinematic viscosity. Moreover, $\omega_L^2(Q)$ has the low-Q dependence on Q^2 given by $\omega_L^2(Q) = c_L^2 Q^2$, where c_L equals the $Q\to 0$ value of the infinite-frequency sound velocity $c_\infty(0)$.[50] Then, the relationship $1/\tau_0 = (c_L^2 - c_s^2)/\nu$ provides in Eq. (11) a first term such as to give the same amount of "total memory," i.e., the same time integral $M_{int}(Q) = \int_0^\infty dt M(Q,t)$ as in the hydrodynamic case.[50,59] Equation (11) produces a four-line shape at any nonzero Q, but the amplitude I_2 can be shown to vanish for $Q\to 0$ (Ref. 59) so as to tend to the hydrodynamic three-line spectrum which is similar to Eq. (9) but lacks the second central line (that is, with $I_2=0$).

TABLE I. $Q\rightarrow 0$ behavior of the parameters in the viscoelastic memory function.

Parameter	$Q\rightarrow 0$ limit	Definitions
$\gamma(Q)$	$\gamma_0=c_p/c_v$	c_p and c_v specific heat at constant pressure and volume, respectively
$\Gamma_T(Q)$	$\gamma_0 D_T Q^2$	D_T thermal diffusivity[a]
$\langle\omega_Q^2\rangle$	$\langle\omega_0^2\rangle=c_s^2Q^2/\gamma_0$	c_s adiabatic sound velocity
$\Delta_L^2(Q)$	$(c_L^2-c_s^2)Q^2$	$c_L=c_\infty(0)$
$1/\tau(Q)$	$1/\tau_0=(c_L^2-c_s^2)/\nu$	ν kinematic longitudinal viscosity[a]

[a]Reference 50.

Thus, VE model (7) complies with the linearized-hydrodynamic predictions for $Q\rightarrow 0$ but retains the presence of the relaxation time τ which is a characteristic feature of the concept of viscoelasticity. The various parameters of Eq. (7) and their $Q\rightarrow 0$ behavior in terms of thermodynamic and transport properties of the fluid are summarized in Table I. The leading terms in the $Q\rightarrow 0$ dependence of the parameters of spectrum (9) are collected in Table II.[59]

Expression (7) is the extension of memory function (11) to higher Q values, obtained by allowing for an unconstrained Q dependence of its coefficients. For example, γ_0, $\gamma_0 D_T Q^2$, and τ_0 are generalized to $\gamma(Q)$, $\Gamma_T(Q)$, and $\tau(Q)$, respectively (see Table I). In this way, a dynamical model is obtained which may prove adequate in the whole Q range between the lowest-Q values attainable with neutron or x-ray spectroscopies (i.e., a few nm^{-1}) and $Q\approx Q_p$ at least. Actually, as already recalled, we showed in the methane case[41] that the generalization of Eq. (11) embodied in VE model (7) provides a description of coherent dynamical spectra that is valid up to very large Q's. Here, however, we will apply it in the range between 2 and 17 nm^{-1} actually probed by the INS experiment, that is, to values up to about Q_p.

A. Results

Line shape (9) derived from VE model (7) was fitted, at each Q, to the $S_{CC}(Q,\omega)$ data for CO_2 letting $S_{CC}(Q)$, z_1, z_2, z_s, ω_s, and I_1 be free parameters. From these, I_2 can be obtained in the way explained in the Appendix, while b_s is found from its expression already given above. The various parameters of memory function (7) can also be calculated from the fitted quantities as shown in the Appendix. The fit range included all data points up to the frequency where $S_{CC}(Q,\omega)$ has decayed below 10^{-3} times the peak ($\omega=0$) value. The quality of the fit is very good at all the studied Q values. The comparison of best-fit spectral shapes or, equivalently, of the Q behavior of the parameters of $M(Q,t)$ or $S_{CC}(Q,\omega)$, with those obtained by the use of Eq. (11), can show to what extent and at which Q values it becomes necessary to allow for the generalization brought about in passing from Eq. (11) to Eq. (7).

TABLE II. $Q\rightarrow 0$ behavior of the parameters in the viscoelastic line shape of Eq. (9).

Parameter	$Q\rightarrow 0$ limit
$I_1(Q)$	$1-1/\gamma_0$
$z_1(Q)$	$D_T Q^2$
$I_2(Q)$	$(\nu\tau_0^3 c_s^2/\gamma_0)Q^4$
$z_2(Q)$	$1/\tau_0$
$z_s(Q)$	$[\nu+(\gamma_0-1)D_T]Q^2/2$
$\omega_s(Q)$	$c_s Q$

TABLE III. Thermodynamic and transport properties of the CO_2 sample (Ref. 43).

ρ	1160 kg m^{-3}	Mass density
γ_0	2.03	Specific-heat ratio
λ	0.174 W m^{-1} K^{-1}	Thermal conductivity
c_p	1964.6 J kg^{-1} K^{-1}	Specific heat at constant pressure
η_s	235.0×10^{-6} Pa s	Shear viscosity
η_b	193.7×10^{-6} Pa s	Bulk viscosity[a]
$\nu=[(4/3)\eta_s+\eta_b]/\rho$	4.37×10^{-7} m^2 s^{-1}	Kinematic longitudinal viscosity
$D_T=\lambda/\rho c_p$	7.63×10^{-8} m^2 s^{-1}	Thermal diffusivity
c_s	939.68 m s^{-1}	Adiabatic sound speed

[a]Reference 61.

The spectral distributions produced by Eq. (11) can, in fact, be evaluated numerically without any approximation since, apart from τ_0, all needed quantities are either thermophysical properties available in the literature[43,61] or derived from them. Their values for CO_2 in the thermodynamic state of the present work are collected in Table III. As for the relaxation time, we take $1/\tau_0=9.77$ ps^{-1}, obtained as described later.

We thus begin by comparing in Fig. 5 one of our lowest-Q MD spectra ($Q=3$ nm^{-1}) with the calculated line shape prescribed by Eq. (11) and with that obtained from the fitting analysis. The $Q\rightarrow 0$ limit model [Eq. (11)] clearly reveals its inadequacy, and the free Q dependence of the memory function parameters enabled by the use of Eq. (7) appears to be necessary.

The adequacy of VE model (7) to reproduce MD data is not restricted to such low-Q values. In Fig. 5 the very good agreement between simulated and fitted spectra is also shown, as an example, for two more Q values for which the calculation based on Eq. (11) is surely inapplicable and is not shown. The quality of the fit is also indirectly shown by the agreement of the fitted CM static structure factor (Fig. 6) with the one obtained by frequency integrating the spectra. $S_{CC}(Q)$ displays at low Q the shallow minimum typical of the liquid phase following an initial decrease in the thermodynamic value of $S_{CC}(0)$.

In the following, we first report the Q dependence of the various parameters of memory function (7). In Fig. 7(a) we display $\omega_L^2(Q)$ together with its parabolic low-Q behavior obtained from the best fitting of $\omega_L^2(Q)=c_L^2Q^2$ in the range of $Q\leq 3$ nm^{-1}, with the result $c_L=2.27\pm 0.02$ nm/ps. This value, together with the relationship $1/\tau_0=(c_L^2-c_s^2)/\nu$, has

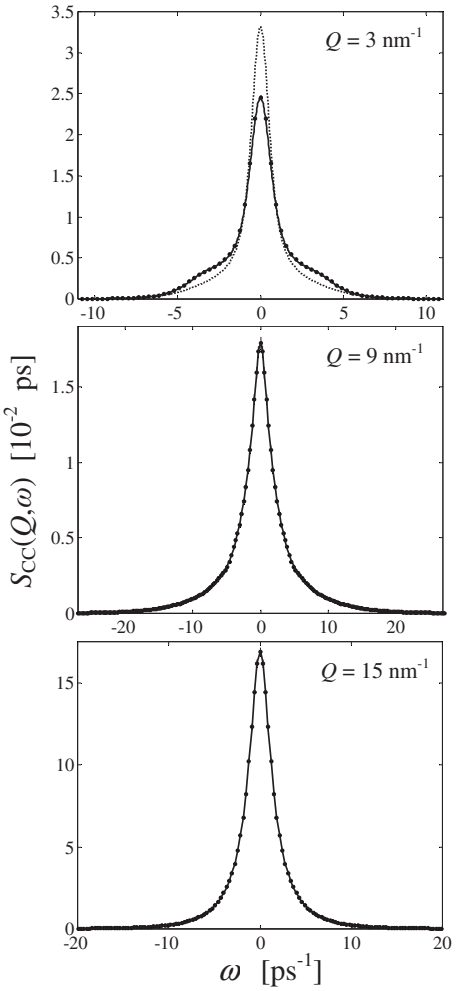

FIG. 5. Simulated $S_{CC}(Q,\omega)$ from the EPM2 potential (dots with error bars) and best-fit curves (solid lines) obtained with viscoelastic model (9) at three Q values. At $Q=3$ nm^{-1}, the spectrum calculated from memory function (11) is also shown as a dotted line. The calculated spectrum has been convoluted with the MD resolution function and normalized so as to have a frequency integral equal to the fitted $S_{CC}(Q)$.

provided the already quoted estimate of $1/\tau_0$. In Fig. 7(b), $\langle\omega_Q^2\rangle$ is shown to be in very good agreement with its theoretical value $k_BTQ^2/mS_{CC}(Q)$; and the deviation from the quadratic behavior $c_s^2Q^2/\gamma_0$, also displayed, reveals the effect of the Q dependence of the static structure factor and, in particular, first, its low-Q decrease and, further, its rapid growth towards the maximum at Q_p.

Figure 8 reports the Q dependence of the other parameters of the memory function. Figure 8(a) shows that $\gamma(Q)$ is characterized by an initial increase over the thermodynamic value γ_0 followed by a sudden decrease that brings it close to unity. Such a behavior was also found in the case of methane.[41] The remaining panels of Fig. 8 report, for the two exponential terms of Eq. (7), the time decay coefficients, the amplitudes, and the contributions to the integrated memory $M_{int}(Q)=M_{1,int}(Q)+M_{2,int}(Q)$ with $M_{1,int}(Q)=\tau(Q)\Delta_L^2(Q)$ and $M_{2,int}(Q)=[\gamma(Q)-1]\langle\omega_Q^2\rangle/\Gamma_T(Q)$. The values of $1/\tau_0$, γ_0, and $(\gamma_0-1)c_s^2Q^2/\gamma_0^2D_T$ are also shown as the $Q=0$ points

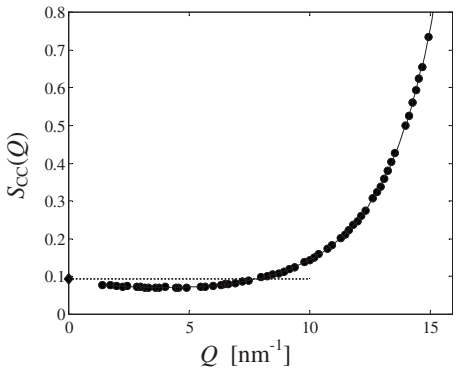

FIG. 6. Center-of-mass static structure factor $S_{CC}(Q)$ of liquid CO_2 from the VE fits (full circles) and from frequency integration (solid line) of the EPM2-based simulated spectra. The dotted line shows the level of the thermodynamic $S_{CC}(0)$ limit (full diamond at $Q=0$) as derived from PVT data (Ref. 43).

in the plots of $1/\tau(Q)$, $\gamma(Q)$, and $M_{2,int}(Q)$. Lines represent the parabolic low-Q behavior of the other quantities.

Figure 9 displays the fit results for the Q dependence of the widths and amplitudes of the central lines of spectrum (9). These are shown together with their low-Q limit behavior calculated in Ref. 59 and reported in Table II.

Finally, we report the results for the parameters of the inelastic spectral lines of Eq. (9). As demonstrated in Ref. 59, the excitation frequency ω_s can be identified, at each Q, with the oscillation frequency of a damped harmonic oscillator having a characteristic (undamped) frequency Ω so that

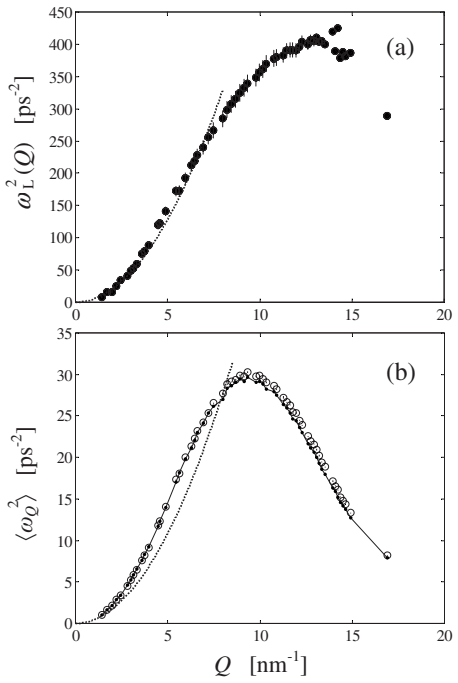

FIG. 7. (a) Fitted ω_L^2 (full circles) as a function of Q compared with the parabola (dotted line) $c_L^2Q^2$ with $c_L=2.27$ nm/ps. (b) Fitted normalized second frequency moment $\langle\omega_Q^2\rangle$ (open circles). The solid line linking full dots is the theoretical prescription $k_BTQ^2/mS_{CC}(Q)$ where the fitted $S_{CC}(Q)$ is used. The dotted curve is the $Q\to0$ limit $c_s^2Q^2/\gamma_0$.

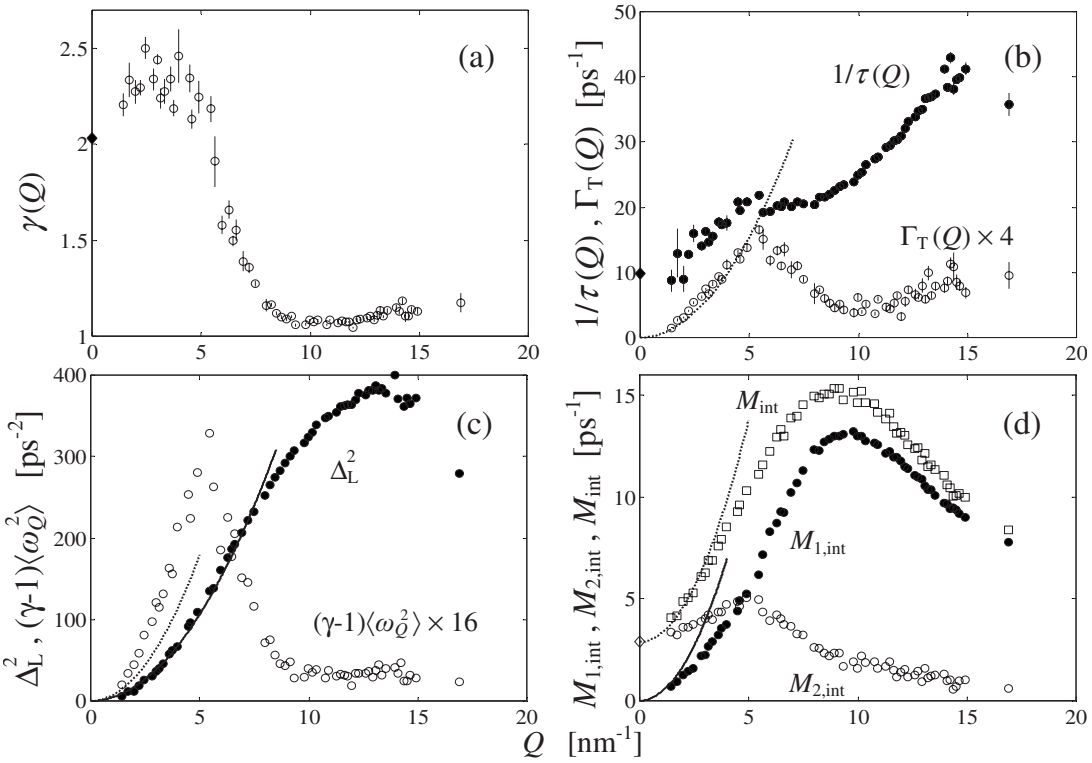

FIG. 8. Relevant quantities in VE memory function (7) calculated from the best-fit parameters of the MD spectra (EPM2 model). (a) Generalized specific-heat ratio $\gamma(Q)$; the $Q=0$ value γ_0 is shown as a full diamond. (b) Inverse time constants of the two exponential terms of Eq. (7): $1/\tau(Q)$ (full circles), estimated (see text) $1/\tau_0$ value (full diamond at $Q=0$), Γ_T (open circles), and its limiting $Q\to 0$ trend (dotted line). Both latter curves are multiplied by a factor of 4. (c) Amplitudes of the two exponential terms in memory function (7): $\Delta_L^2(Q)$ (full circles) and $[\gamma(Q)-1]\langle\omega_Q^2\rangle$ (open circles) are compared with their $Q\to 0$ behaviors (solid and dotted lines, respectively). The curves for $[\gamma(Q)-1]\langle\omega_Q^2\rangle$ are multiplied by a factor of 16. (d) Time integrals of the two terms in memory function (7) $M_{1,\mathrm{int}}(Q)$ (full circles), $M_{2,\mathrm{int}}(Q)$ (open circles), and their sum $M_{\mathrm{int}}(Q)$ (squares). The solid and dotted lines are the low-Q parabolic behavior of $M_{1,\mathrm{int}}(Q)$ and $M_{\mathrm{int}}(Q)$. The diamond is the $Q=0$ value of $M_{2,\mathrm{int}}(Q)$.

$$\omega_s = \sqrt{\Omega^2 - z_s^2}. \tag{12}$$

Here, all quantities are functions of Q, with

$$\Omega(Q) = \sqrt{\gamma(Q)\langle\omega_Q^2\rangle / r(Q)}, \tag{13}$$

where the renormalization function $r(Q)$ in the VE case takes the form[59]

$$r(Q) = \frac{z_1 z_2 \gamma(Q)\tau(Q)}{\Gamma_T(Q)}. \tag{14}$$

As long as Ω remains larger than z_s, the damped harmonic oscillator is in the so-called undercritical damping state, corresponding to the presence of propagating acoustic excitations in the liquid. From the results shown in Fig. 10(a), where the Q dependence of Ω and z_s is displayed, we can conclude that such a situation is found in liquid CO_2 up to Q values close to 14 nm^{-1}, where the critical damping condition, where $\omega_s=0$, is reached, as shown in Fig. 10(b). Above this value overdamping takes place, causing a loss of wave propagation at the highest wave vectors investigated here. This happens when the two complex roots z_A and z_B turn into real distinct quantities so that ω_s, defined as their imaginary part, sticks at zero.

In the overdamped regime, characterized by $\Omega < z_s$, Eq. (12) loses its validity. Indeed, the general expressions of Ω and z_s, valid at any Q, are $\Omega=\sqrt{z_A z_B}$ and $z_s=-(z_A+z_B)/2$ [the former reducing to Eq. (12) in the underdamped case]. With real z_A and z_B spectrum (9) changes into the sum of four central Lorentzians, while intermediate scattering function (10) is accordingly modified into the sum of four exponentially decaying terms, where the disappearance of any oscillatory feature of $F_{CC}(Q,t)$ signals the absence of propagating excitations.

B. Discussion

From the results collected in Figs. 7–10, it appears that the discussion of the collective dynamics of liquid CO_2 is better carried out if different Q ranges are considered separately.

We begin by considering the data up to $Q\approx 5$ nm^{-1}. A first observation regards the consistency of the MD data with the $Q\to 0$ thermodynamic and transport properties of the fluid. This demonstrates, in particular, that the used interaction potential quite effectively reproduces the thermophysical properties of liquid CO_2. In the low-Q limit, the overall behavior is in qualitative agreement with the dynamics predicted by model (11). However, we already remarked (see

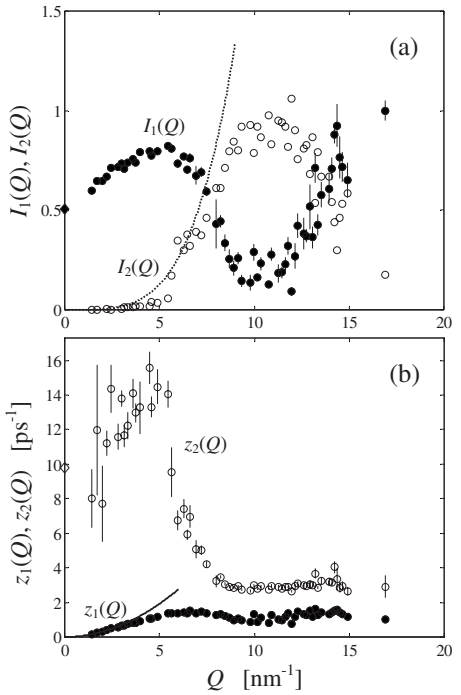

FIG. 9. (a) Amplitudes and (b) half widths at half maximum of the two central Lorentzians from VE fitting [Eq. (9)] of MD spectra (symbols), compared with their respective low-Q trends (lines) or $Q=0$ values (diamonds). In (a), I_1 (full circles and diamond) and I_2 (open circles and dotted line). In (b), z_1 (full circles and solid line) and z_2 (open circles and diamond).

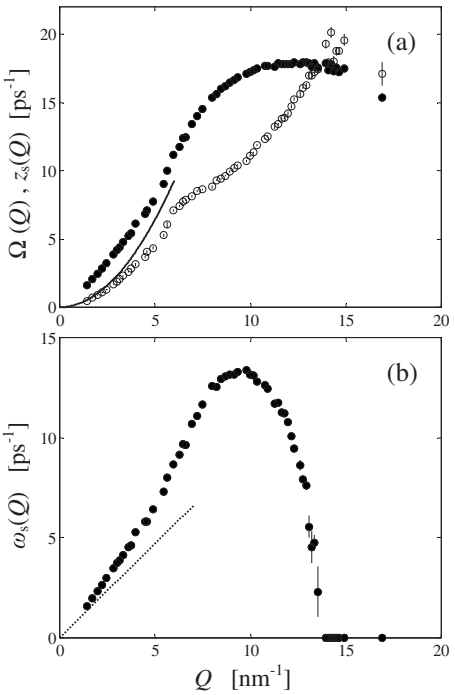

FIG. 10. (a) Q dependence of the undamped frequency $\Omega(Q)$ (full circles) of the VE equivalent harmonic oscillator (see text) and of the damping z_s (open circles) of collective excitations. The line shows the low-Q quadratic behavior of z_s. (b) Dispersion curve of collective excitations. The frequency ω_s (full circles) and the low-Q straight line c_sQ (dashes) are shown.

Fig. 5) that the shape of the spectrum can be exactly reproduced only by allowing for a Q dependence of some of the memory function parameters. In particular, although $\gamma(Q)$ extrapolates smoothly towards its $Q=0$ value, it quickly grows up to about 20% over γ_0, strengthening the role played by the second term in $M(Q,t)$ [Figs. 8(c) and 8(d)]. The inverse relaxation time $1/\tau(Q)$ also increases over $1/\tau_0$, determining an analogous initial growth of z_2.

The damping z_s of the acoustic modes rather soon deviates from its low-Q expression. Moreover, already at the lowest Q, the dispersion curve stays above the linear $Q\rightarrow 0$ behavior characterized by the adiabatic sound speed [the straight line in Fig. 10(b)]. Such a deviation has two causes: one, of static nature, is the initial decrease in the structure factor $S_{CC}(Q)$, which makes $\langle\omega_Q^2\rangle$ grow faster than Q^2; the other, that will be commented on later, is a characteristic dynamical effect of the viscoelastic modeling due to the presence of the relaxation time $\tau(Q)$. Both induce a stronger increase in the excitation frequency than what is predicted in a hydrodynamic framework.

A quite different overall picture is obtained in the Q range between about 5 and 10 nm^{-1}. The most evident fact here is the sudden loss of importance of the quantities related to the "thermal" part of the memory function. $\gamma(Q)$ drops to values quite close to unity, while $\Gamma_T(Q)$ and z_1 stop their initial quadratic growth. The simultaneous drop of the width (z_2) and the strong increase in the amplitude (I_2) of the second central Lorentzian line make this nonpropagating "relaxation" mode become the dominant contribution to the quasi-elastic part of the spectrum. Indeed, while the amplitude I_2 is practically negligible up to $Q\approx 5$ nm^{-1}, the weight of the two central lines is almost interchanged in this intermediate Q range [see Fig. 9(a)].

The effect of $S_{CC}(Q)$ on the normalized second moment begins now to be reversed since the static structure factor grows quickly above its $Q=0$ value. $\langle\omega_Q^2\rangle$ has an inflection point and starts to bend downwards, reaching a maximum and then clearly decreasing. A similar behavior is displayed by $\omega_L^2(Q)$, $\Delta_L^2(Q)$, and the integrated memory $M_{\text{int}}(Q)$. As for $\Omega(Q)$, it also shows a negative curvature but stays at a nearly constant level beyond the maximum. As it can be appreciated from Eqs. (13) and (14), this is, again, the result of the two combined effects, mentioned before, that now compensate each other. Indeed, while the drop of $\langle\omega_Q^2\rangle$ due to the rising static structure factor tends to lower $\Omega(Q)$, an opposite effect is produced by the decrease in $\tau(Q)$, which reduces $r(Q)$. [In Eq. (14), $\tau(Q)$ is the quantity with the strongest variation above $Q\approx 10$ nm^{-1}.] On the other hand, although z_s displays an evident change in slope around 6 nm^{-1} [see Fig. 10(a)], it keeps growing until it exceeds the value of $\Omega(Q)$.

By means of Eq. (12), a complete description of the shape of the dispersion curve can be obtained in terms of structural and dynamical properties of the system. In the viscoelastic framework, the propagation speed of acoustic excitations is expected to undergo a transition from the low-Q adiabatic value c_s to the higher value of the infinite-frequency speed c_∞. The rationale behind such a prediction is the fact that when the excitation frequency becomes too high with respect

to the inverse of the (dominant) relaxation time, the relaxation mechanism quickly loses effectiveness, giving the system its "elastic" character. If, with increasing Q, the relaxation time becomes shorter [i.e., $1/\tau(Q)$ increases] then, on the one hand, the occurrence of such a transition is pushed towards higher-Q values, while, on the other hand, the growth of the damping z_s tends to reduce the excitation frequency. Both effects first cooperate in limiting the mentioned increase in the propagation speed and, with further increasing Q, bring the acoustic oscillations into the overdamping condition and cause the consequent arrest of the propagation in a rather narrow range around Q_p. This is the most evident feature of the dispersion curve at the highest-Q values here considered. In this respect, Fig. 10(b) resembles very closely the analogous picture obtained in Refs. 41 and 60 for liquid methane, confirming that such a dynamical behavior, also previously found in monatomic systems,[62] may be a typical property of dense liquids.

VI. FINAL COMMENTS

We presented a comprehensive report about the dynamics of liquid CO_2, ranging from the determination of reliable interaction potentials to the characterization of collective modes, through a detailed analysis of the inelastic neutron scattering measurements and MD simulations performed for this system.

Various site-site potentials have been investigated by comparing the MD predictions with the first experimental data for the dynamic structure in a Q range extending up to about Q_p. Good overall quality of four over six models is found, and some indication is obtained of an advisable use of the EPM2 potential. In this sense, the first part of this work constitutes an experimental validation, through INS, of the EPM2-based simulation data. This result has then made it possible to achieve determination of the dynamics of collective modes by analyzing in detail the center-of-mass dynamic structure factor $S_{CC}(Q,\omega)$ with the application of the concepts described in detail in Ref. 59.

A viscoelastic modeling of the CM spectra was found to provide an accurate description of the frequency distributions at all Q's. The dynamical behavior is consistent, but only in the $Q \to 0$ limit, with the one predicted by hydrodynamic theory, and reveals the important role played, up to $Q \approx 5$ nm^{-1}, by thermal effects, mostly evidenced by the variation in $\gamma(Q)$. In this low-Q part of our studied wave-vector range, the negligible value of I_2 shows that the system can be assumed to behave in a hydrodynamiclike way, provided that the thermophysical properties of the fluid are allowed to follow a generalized Q dependence. In this respect, it is worth noting that a Q value of 5 nm^{-1} corresponds to an excitation wavelength of about 3σ, meaning that the liquid already approaches the continuum limit when probed over distances as short as only three molecular diameters.[63]

On the other hand, beyond such a Q value, a sort of rather abrupt transition appears in the behavior of all the quantities entering the definition of either memory function (7) or spectrum shape (9). In the first term of Eq. (7), becoming the dominant one, the presence of an exponential relaxation with a decay time $\tau(Q)$ adequately models the viscoelastic response shown by the liquid dynamics.

The shape of the dispersion curve is determined by the combined action of z_s and Ω, which are the two parameters that define, at each Q, the state of the equivalent damped harmonic oscillator representing the sound mode. The resulting excitation frequency shows, as a function of Q, the effects of the Q dependence of $1/\tau$, S_{CC}, and z_s. In particular, $\omega_s(Q)$ displays both an initial increase in the linear behavior $c_s Q$ and the pronounced drop beyond $Q \approx 10$ nm^{-1} typically found in simple dense liquids. In particular, liquid CO_2 turns out to be another case where the acoustic waves cease to propagate when Q approaches Q_p.

A more than qualitative agreement is thus found between the dynamical behaviors of different molecular liquids so far investigated in detail, such as carbon dioxide and methane. The present work highlights the effectiveness of combined efforts aiming at the experimental determination of dynamic structure factors, the simulation of center-of-mass dynamics with valid potential models, and the analysis of spectra based on the applications of unified rigorous criteria for the assessment of energy and damping of the collective modes in liquids.

ACKNOWLEDGMENTS

We wish to thank R. Favillini, F. Formisano, A. Orecchini, M. Jiménez-Ruiz, and the ILL personnel for their precious contributions to the neutron measurements. We acknowledge the collaboration of G. Venturi during the raw neutron-data preliminary treatment. We acknowledge the courtesy of the authors of Ref. 55 for providing the correct potential parameters.

APPENDIX

We recall here from Ref. 59 a few useful properties of viscoelastic model (7). Using Eq. (8), the amplitudes of the various spectral lines can be obtained as

$$I_j = \frac{V(z_j)}{\prod_{k \neq j} (z_j - z_k)},$$

where $j,k = A,B,C,D$ refer to the four zeros of $W(z)$ (see text). For the central lines, this leads to

$$I_1 = I_C = \frac{-z_A z_B z_D}{(z_C - z_A)(z_C - z_B)(z_C - z_D)} \left[1 - \frac{z_C(z_A + z_B + z_D)}{\Gamma_T(Q)/\tau(Q)} \right] \tag{A1}$$

and, with cyclic permutation of the indices,

$$I_2 = I_D = \frac{-z_B z_C z_A}{(z_D - z_B)(z_D - z_C)(z_D - z_A)} \left[1 - \frac{z_D(z_B + z_C + z_A)}{\Gamma_T(Q)/\tau(Q)} \right]. \tag{A2}$$

The above, and all subsequent formulas in this appendix, are valid for both complex conjugate and real z_A and z_B. One can solve Eq. (A1) for $\Gamma_T(Q)/\tau(Q)$ using the fitted value of I_1

and substitute it into Eq. (A2) to obtain I_2 and the formula for b_s given in Sec. V. Moreover, I_s is obtained from the sum rule $I_1+I_2+2I_s=1$.

Once all the parameters of spectrum (9) are known through either the fit or the above expressions, the memory function parameters can be derived by exploiting the properties of the roots of a polynomial equation. If the fourth-degree polynomial $W(z)$ is written as

$$W(z) = z^4 + g_1 z^3 + g_2 z^2 + g_3 z + g_4,$$

one has

$$g_1 = -(z_A + z_B + z_C + z_D),$$

$$g_2 = z_A z_B + (z_A + z_B)(z_C + z_D) + z_C z_D,$$

$$g_3 = -[z_A z_B (z_C + z_D) + (z_A + z_B) z_C z_D],$$

$$g_4 = z_A z_B z_C z_D,$$

where all quantities are functions of Q. For viscoelastic memory function (7)

$$g_1 = \frac{1}{\tau(Q)} + \Gamma_T(Q),$$

$$g_2 = \frac{\Gamma_T(Q)}{\tau(Q)} + \omega_L^2(Q),$$

$$g_3 = \omega_L^2(Q)\Gamma_T(Q) + \langle \omega_Q^2 \rangle \left\{ \frac{\gamma(Q)}{\tau(Q)} - [\gamma(Q) - 1]\Gamma_T(Q) \right\},$$

$$g_4 = \langle \omega_Q^2 \rangle \frac{\Gamma_T(Q)}{\tau(Q)}.$$

We also use in the following the relations $\Omega^2 = z_A z_B$ and $z_s = -(z_A + z_B)/2$.

$\Gamma_T(Q)$ and $1/\tau(Q)$ can be calculated as the solutions of a quadratic equation. By taking their product P from Eq. (A1),

$$P = \frac{\Gamma_T(Q)}{\tau(Q)} = z_C(z_D - 2z_s)\left[1 + \frac{I_1(z_C^2 + 2z_s z_C + \Omega^2)}{\Omega^2 z_D} \right]^{-1},$$

and their sum S from the two above expressions of g_1,

$$S = \Gamma_T(Q) + \frac{1}{\tau(Q)} = z_C + z_D - 2z_s,$$

the equation $x^2 - Sx + P = 0$ is obtained and easily solved. Moreover, the two expressions of g_4 give $\langle \omega_Q^2 \rangle$ as

$$\langle \omega_Q^2 \rangle = \frac{\Omega^2 z_C z_D}{\Gamma_T(Q)/\tau(Q)},$$

while those of g_2 and of g_3 yield $\omega_L^2(Q)$ and $\gamma(Q)$, respectively, with the results

$$\omega_L^2(Q) = \Omega^2 - 2z_s(z_C + z_D) + z_C z_D - \frac{\Gamma_T(Q)}{\tau(Q)},$$

$$\gamma(Q) = \frac{1}{\Gamma_T(Q) - \frac{1}{\tau(Q)}} \left\{ \frac{1}{\langle \omega_Q^2 \rangle} [\Omega^2(z_C + z_D) + 2z_s z_C z_D - \omega_L^2(Q)\Gamma_T(Q)] + \Gamma_T(Q) \right\}.$$

Alternatively, $\langle \omega_Q^2 \rangle$ and $\omega_L^2(Q)$ can be calculated by noting that Eq. (10) can be written as

$$\frac{F(Q,t)}{F(Q,0)} = \sum_j I_j \exp(z_j |t|),$$

and using the well-known relation between the zero-time properties of $F(Q,t)$ and the moments of the corresponding classical symmetric spectrum $S(Q,\omega)/S(Q)$,

$$\left[\frac{d^k}{dt^k} \left(\frac{F(Q,t)}{F(Q,0)} \right) \right]_{t=0} = i^k \langle \omega_Q^k \rangle,$$

which in the viscoelastic case is applicable with $k \leq 4$. For $k=2$, this gives

$$\langle \omega_Q^2 \rangle = -\sum_j I_j z_j^2,$$

while for $k=4$

$$\omega_L^2(Q) = \frac{\langle \omega_Q^4 \rangle}{\langle \omega_Q^2 \rangle} = \frac{1}{\langle \omega_Q^2 \rangle} \sum_j I_j z_j^4.$$

[1] E. Guarini, U. Bafile, F. Barocchi, F. Demmel, F. Formisano, M. Sampoli, and G. Venturi, Europhys. Lett. **72**, 969 (2005).

[2] F. Sette, G. Ruocco, A. Cunsolo, C. Masciovecchio, G. Monaco, and R. Verbeni, Phys. Rev. Lett. **84**, 4136 (2000).

[3] P. Giura, R. Angelini, F. Datchi, G. Ruocco, and F. Sette, J. Chem. Phys. **127**, 084508 (2007).

[4] K. Carneiro and J. P. McTague, Phys. Rev. A **11**, 1744 (1975).

[5] K. S. Pedersen, K. Carneiro, and F. Y. Hansen, Phys. Rev. A **25**, 3335 (1982).

[6] F. Bencivenga, A. Cunsolo, M. Krisch, G. Monaco, L. Orsingher, G. Ruocco, F. Sette, and A. Vispa, Phys. Rev. Lett. **98**, 085501 (2007).

[7] J. Teixeira, M. C. Bellissent-Funel, S. H. Chen, and B. Dorner, Phys. Rev. Lett. **54**, 2681 (1985).

[8] G. Ruocco and F. Sette, J. Phys.: Condens. Matter **11**, R259 (1999), and references therein.

[9] C. Petrillo, F. Sacchetti, B. Dorner, and J.-B. Suck, Phys. Rev. E **62**, 3611 (2000); F. Sacchetti, J.-B. Suck, C. Petrillo, and B. Dorner, *ibid.* **69**, 061203 (2004).

[10] F. J. Bermejo, F. Batallan, J. L. Martínez, M. Garcia-Hernández, and E. Enciso, J. Phys.: Condens. Matter **2**, 6659 (1990); J. Alonso, F. J. Bermejo, M. Garcia-Hernández, J. L. Martínez, W. S. Howells, and A. Criado, J. Chem. Phys. **96**, 7696 (1992).

[11] K. Yoshida, N. Yamamoto, S. Hosokawa, A. Q. R. Baron, and T.

Yamaguchi, Chem. Phys. Lett. **440**, 210 (2007).
[12] F. J. Bermejo, J. L. Martínez, D. Martín, M. García-Hernández, F. J. Mompeán, and J. Alonso, J. Chem. Phys. **95**, 5387 (1991); J. L. Martínez, F. J. Bermejo, M. García–Hernández, F. J. Mompeán, E. Enciso, and J. Martín, J. Phys.: Condens. Matter **3**, 4075 (1991).
[13] M. García-Hernández, J. L. Martínez, F. J. Bermejo, A. Chahid, and E. Enciso, J. Chem. Phys. **96**, 8477 (1992).
[14] R. Angelini, P. Giura, G. Monaco, G. Ruocco, F. Sette, and R. Verbeni, Phys. Rev. Lett. **88**, 255503 (2002); R. Angelini, P. Giura, D. Fioretto, G. Monaco, G. Ruocco, and F. Sette, Phys. Rev. B **70**, 224302 (2004).
[15] F. Fernandez-Alonso, S. E. McLain, J. W. Taylor, F. J. Bermejo, I. Bustinduy, and M. D. Ruiz-Martín, J. Chem. Phys. **126**, 234509 (2007).
[16] F. Barocchi, M. Zoppi, and P. A. Egelstaff, Phys. Rev. A **31**, 2732 (1985).
[17] H. Fredrikze, J. B. van Tricht, A. A. van Well, R. Magli, P. Chieux, and F. Barocchi, Phys. Rev. Lett. **62**, 2612 (1989).
[18] F. Barocchi, P. Chieux, R. Magli, L. Reatto, and M. Tau, Phys. Rev. Lett. **70**, 947 (1993).
[19] R. Magli, F. Barocchi, P. Chieux, and R. Fontana, Phys. Rev. Lett. **77**, 846 (1996).
[20] F. Formisano, C. J. Benmore, U. Bafile, F. Barocchi, P. A. Egelstaff, R. Magli, and P. Verkerk, Phys. Rev. Lett. **79**, 221 (1997).
[21] F. Formisano, F. Barocchi, and R. Magli, Phys. Rev. E **58**, 2648 (1998).
[22] E. Guarini, G. Casanova, U. Bafile, and F. Barocchi, Phys. Rev. E **60**, 6682 (1999).
[23] E. Guarini, G. Casanova, U. Bafile, F. Formisano, R. Magli, and F. Barocchi, Europhys. Lett. **49**, 62 (2000).
[24] E. Guarini, R. Magli, M. Tau, F. Barocchi, G. Casanova, and L. Reatto, Phys. Rev. E **63**, 052201 (2001).
[25] P. Verkerk, U. Bafile, F. Barocchi, L. A. de Graaf, J.-B. Suck, and H. Mutka, Phys. Rev. Lett. **67**, 1262 (1991).
[26] L. E. Bove, F. Sacchetti, C. Petrillo, B. Dorner, F. Formisano, and F. Barocchi, Phys. Rev. Lett. **87**, 215504 (2001).
[27] L. E. Bove, F. Formisano, F. Sacchetti, C. Petrillo, A. Ivanov, B. Dorner, and F. Barocchi, Phys. Rev. B **71**, 014207 (2005).
[28] M. D. Ruiz-Martín, M. Jiménez-Ruiz, M. Plazanet, F. J. Bermejo, R. Fernández-Perea, and C. Cabrillo, Phys. Rev. B **75**, 224202 (2007).
[29] J. B. van Tricht, H. Fredrikze, and J. van der Laan, Mol. Phys. **52**, 115 (1984).
[30] A. K. Adya and C. J. Wormald, Mol. Phys. **74**, 735 (1991); **77**, 1217 (1992).
[31] P. Cipriani, M. Nardone, F. P. Ricci, and M. A. Ricci, Mol. Phys. **99**, 301 (2001).
[32] P. A. Egelstaff, D. I. Page, and J. G. Powles, Mol. Phys. **20**, 881 (1971).
[33] T. Bausenwein, H. Bertagnolli, D. Gutwerk, K. Tödheide, and P. Chieux, Mol. Phys. **76**, 127 (1992).
[34] T. Bausenwein, H. Bertagnolli, A. David, K. Goller, and H. Zweier, J. Chem. Phys. **101**, 672 (1994).
[35] M. Zoppi, U. Bafile, E. Guarini, F. Barocchi, R. Magli, and M. Neumann, Phys. Rev. Lett. **75**, 1779 (1995).
[36] G. Strauß, A. Bassen, H. Zweier, H. Bertagnolli, K. Tödheide, A. K. Soper, and J. Turner, Phys. Rev. E **53**, 3505 (1996).
[37] E. Guarini, U. Bafile, F. Barocchi, F. Cilloco, and R. Magli, Mol. Phys. **94**, 289 (1998).
[38] E. Guarini, M. Sampoli, G. Venturi, U. Bafile, and F. Barocchi, Phys. Rev. Lett. **99**, 167801 (2007).
[39] E. Guarini, M. Sampoli, U. Bafile, F. Formisano, M. Jimenéz-Ruiz, A. Orecchini, G. Venturi, and F. Barocchi, Chem. Phys. Lett. **464**, 177 (2008).
[40] A. Habenschuss, E. Johnson, and A. H. Narten, J. Chem. Phys. **74**, 5234 (1981).
[41] M. Sampoli, U. Bafile, F. Barocchi, E. Guarini, and G. Venturi, J. Phys.: Condens. Matter **20**, 104206 (2008).
[42] V. F. Sears, Neutron News **3**, 26 (1992).
[43] E. W. Lemmon, M. O. McLinden, and D. G. Friend, in *Thermophysical Properties of Fluid Systems in NIST Chemistry WebBook*, NIST Standard Reference Database Number 69, edited by P. J. Linstrom and W. G. Mallard (NIST, Gaithersburg, MD, 2005).
[44] C. J. Windsor, *Pulsed Neutron Scattering* (Taylor and Francis, London, 1981).
[45] Institut Laue-Langevin, in *Neutron Data Booklet*, edited by A. J. Dianoux and G. Lander (ILL, Grenoble, 2002), pp. 2.7–3.
[46] E. Guarini, A. Orecchini, F. Formisano, F. Demmel, C. Petrillo, F. Sacchetti, U. Bafile, and F. Barocchi, J. Phys.: Condens. Matter **17**, 7895 (2005).
[47] N. W. Ashcroft and D. C. Langreth, Phys. Rev. **156**, 685 (1967).
[48] E. Guarini and U. Bafile (unpublished).
[49] E. Guarini, J. Phys.: Condens. Matter **15**, R775 (2003).
[50] U. Balucani and M. Zoppi, *Dynamics of the Liquid State* (Clarendon, Oxford, 1994).
[51] D. Fincham, CCP5 Quarterly Report No. 10, 1983, (unpublished), available at http://www.ccp5.ac.uk/ftpfiles/ccp5.newsletters/10/pdf/fincham.pdf; this algorithm was preferred, compared to other more recent methods (see, e.g., http://www.ccp5.ac.uk/infoweb/wsmith4/Euler3.pdf), because of the far better energy conservation obtained in tests of linear rotors under heavy torque.
[52] C. S. Murthy, K. Singer, and I. R. McDonald, Mol. Phys. **44**, 135 (1981); L. C. Geiger, B. M. Ladanyi, and M. E. Chapin, J. Chem. Phys. **93**, 4533 (1990).
[53] J. G. Harris and K. H. Yung, J. Phys. Chem. **99**, 12021 (1995).
[54] S. Tsuzuki and K. Tanabe, Comput. Mater. Sci. **14**, 220 (1999).
[55] S. Bock, E. Bich, and E. Vogel, Chem. Phys. **257**, 147 (2000). The $a^{(5)}=-1.3578\times10^5$ a.u. parameter for the CC interaction was misprinted in Table I of the original paper.
[56] J. J. Potoff and J. I. Siepmann, AIChe J. **47**, 1676 (2001).
[57] Z. Zhang and Z. Duan, J. Chem. Phys. **122**, 214507 (2005).
[58] C. Nieto-Draghi, T. de Bruin, J. Pérez-Pellitero, J. B. Avalos, and A. D. Mackie, J. Chem. Phys. **126**, 064509 (2007).
[59] U. Bafile, E. Guarini, and F. Barocchi, Phys. Rev. E **73**, 061203 (2006).
[60] U. Bafile, F. Barocchi, and E. Guarini, Condens. Matter Phys. **11**, 107 (2008).
[61] The bulk viscosity was estimated as that of the liquid in coexistence at the temperature of our sample, was read off from Fig 4 of K. Rah and B. C. Eu, J. Chem. Phys. **114**, 10436 (2001).
[62] I. M. de Schepper, P. Verkerk, A. A. van Well, and L. A. de Graaf, Phys. Rev. Lett. **50**, 974 (1983).
[63] We take $\sigma=0.4$ nm, i.e. the value of the isotropic collision parameter given in J. O. Hirschfelder, C. F. Curtiss, and R. B. Bird, *Molecular Theory of Gases and Liquids* (Wiley, New York, 1954).